Perpendicular Magnetic Anisotropic $NiCo_2O_4$ Epitaxial Films with Tunable Coercivity

Zhongnan Xi,[1] Yao Li,[1] Pengxiang Hou,[1] Peijie Jiao,[1] Honghe Ding,[2] Fengchun Hu,[2] Jun Hu,[2] Yu Deng,[1] Yurong Yang,[1] and Di Wu[1,*]

[1] *National Laboratory of Solid State Microstructures, Jiangsu Key Laboratory of Artificial Functional Materials, and Department of Materials Science and Engineering, Nanjing University, Nanjing 210093, China*

[2] *National Synchrotron Radiation Laboratory, University of Science and Technology of China, Hefei 230029, China*

(Received 14 February 2022; revised 25 May 2022; accepted 17 June 2022; published 5 July 2022)

Ferrimagnetic $NiCo_2O_4$ (NCO) films with perpendicular magnetic anisotropy, 12.5 nm in thickness, are epitaxially deposited on (001) $MgAl_2O_4$ single-crystalline substrates by pulsed laser deposition. It is observed that the coercive field of the NCO films can be tuned systematically by about 20 times, while keeping the large perpendicular magnetic anisotropy, through simply increasing the deposition temperature from 250 to 350 °C. The increase of resistivity and the increase of low-temperature metal-to-insulator transition temperature suggests increased concentration of defects in NCO films deposited at elevated temperatures. The magnetic and transport characteristics are discussed based on a systematic change in cation valence and coordination in NCO films, as revealed by x-ray photoelectron emission and x-ray absorption spectroscopy measurements. The perpendicular magnetic anisotropy with tunable coercivity makes NCO films promising for multifunctional applications.

DOI: 10.1103/PhysRevApplied.18.014008

I. INTRODUCTION

High-performance magnetic materials are essential fundamental materials that support modern technologies. The ability to control magnetic properties such as saturation magnetization (M_s), remanent magnetization, and coercivity (H_c) is critical not only for applications but also for the fundamental understanding of magnetism. Different applications require different H_c [1–4]. In fact, magnetic materials have been divided into two categories, soft magnets with H_c in the range of a few to a few hundreds of oersteds used in switching, sensing, and microwave absorbing applications [3–6], and hard magnets with H_c of a few thousands of oersteds and even larger, useful for electrical-to-mechanical energy conversion, motors, generators, and magnetic resonance imaging devices [3–7]. Specifically in memory applications, different desired amplitudes of H_c are required for different devices. For example, the write and read heads require low coercivity to enable operations at reasonably high frequencies [8,9], while the recording medium must have coercivity low enough to write on but high enough to resist a demagnetizing field and to store the information for as long as possible [8,9].

Transition metal oxides display a rich variety of fascinating electronic, optical, and magnetic properties owing to the complex interaction among charge, spin, orbit, and lattice, holding great promise from both applied and fundamental research points of view [10–14]. Among them, ferrimagnetic $NiCo_2O_4$ (NCO) with inverse spinel structure has attracted increasing attention in recent years for promising functionalities [15–22]. NCO possesses a high Curie temperature (about 400 K), high saturated magnetization, perpendicular magnetic anisotropy (PMA), and high conductivity [15–22]. However, systematic studies of magnetic and transport characteristics of NCO epitaxial thin films are rarely reported.

In this work, we show that the coercivity of NCO epitaxial films can be tuned by about 20 times from 350 to 7300 Oe by simply increasing the deposition temperature (T_g), while maintaining a large PMA. The effective magnetic anisotropy constant (K_{eff}) fluctuates between 1.9 and 5.1 Merg cm^{-3}. The analysis of the temperature dependence of longitudinal resistivity manifests the increased disorder in NCO films, indicating the essential pinning effect of disorder during domain switching. The variation of Curie temperature (T_C), saturated magnetization, and transport characteristics are discussed based on a systematic change in valence and coordination of cations in the NCO films as functions of T_g. Our work provides a simple method to tune the coercivity of NCO films with strong PMA for multifunctional applications.

*diwu@nju.edu.cn

II. EXPERIMENT

NCO films are deposited by pulsed laser deposition on (001)-oriented $MgAl_2O_4$ (MAO) single-crystalline substrates, ultrasonically cleaned in ethanol for 10 min, then in deionized water for 10 min. During deposition, a NCO ceramic target made by conventional solid-state reaction and sintering is ablated with a 248-nm KrF excimer laser (Compex Pro 205, Coherent) at 4 Hz. The power density on the target is 2.5 J cm^{-2}. The oxygen pressure in the chamber is kept at 0.1 mbar, while the substrate temperature is maintained at T_g, which increases from 250 to 350 °C in 25 °C steps. The surface morphology of these films is checked with an atomic force microscope (Cypher ES, Asylum Research). The crystallinity, thickness and lattice constants of the films are measured on a Bruker D8 Discover x-ray diffractometer with Cu $K\alpha 1$ radiation ($\lambda = 1.5406$ Å). Magnetic measurements are carried out on a superconducting quantum interference device magnetometer (MPMS XL-7, Quantum Design). A physical property measurement system (PPMS-9, Quantum Design) is used to measure the transport properties using indium contact electrodes and gold wires in a van der Pauw configuration. X-ray photoelectron spectroscopy (XPS) (K-Alpha, Thermo Scientific) is employed to evaluate the composition and valence states of Ni and Co in the NCO films. X-ray absorption spectra (XAS) are collected in total electron yield mode at room temperature at the MCD-A and MCD-B (Soochow Beamline for Energy Materials) beamlines at the National Synchrotron Radiation Laboratory (Hefei, China).

III. RESULTS AND DISCUSSION

A. Structural characterization

Figure 1(a) shows the θ-2θ x-ray diffraction (XRD) patterns of the NCO films deposited at various T_g, around the (004) reflection of the MAO substrate. Regardless of the T_g, NCO films all exhibit (004) diffraction accompanied with distinct Laue thickness fringes and there are no observable secondary phases from any impurities, indicating the high crystallinity of films with smooth surface and sharp interface. It is clear that the (004) diffraction peak of NCO shifts to lower angles as T_g increases, indicative of an increase in the out-of-plane lattice parameter. As shown in Fig. 1(d), the calculated out-of-plane lattice parameter increases from 8.18 to 8.23 Å as T_g increases from 250 to 350 °C. Lattice parameter variation may be a result of cation nonstoichiometry [23], different coordination, or oxygen deficiency [24,25], which is discussed in the following. Figure 1(b) shows two-dimensional XRD intensity mapping of a NCO film deposited at 350 °C around the (115) reciprocal spot of the MAO substrate as

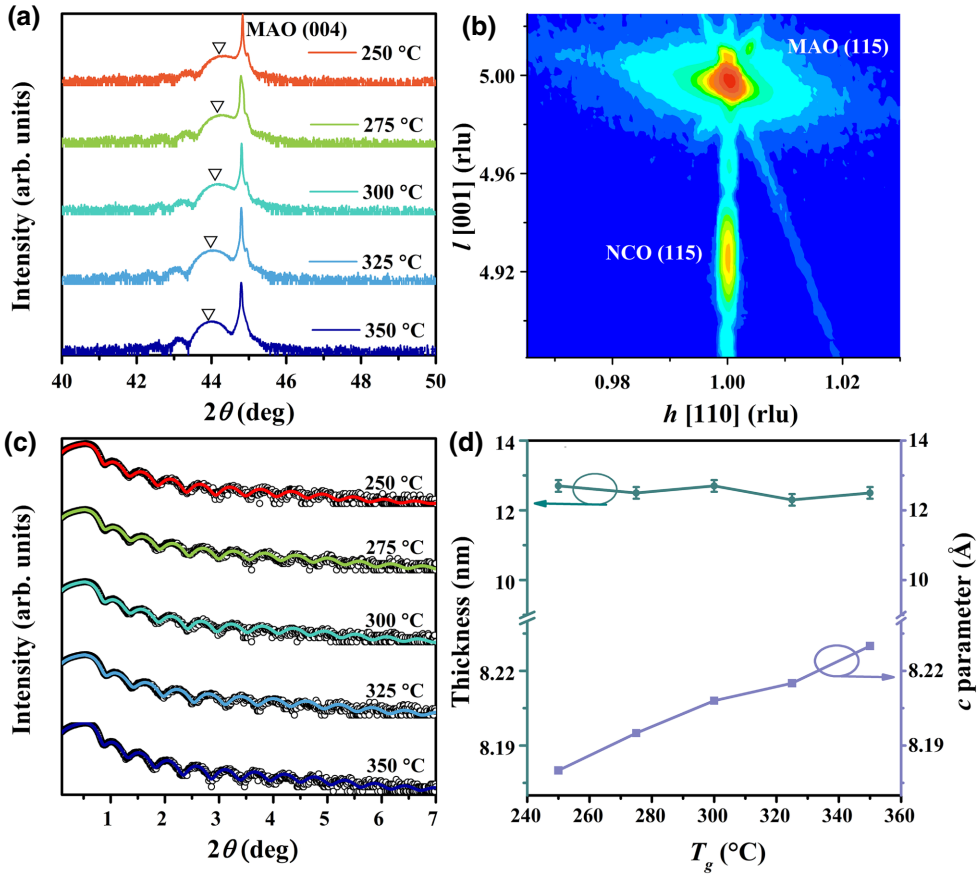

FIG. 1. (a) θ-2θ XRD patterns of NCO films deposited at various T_g. The triangles serve to indicate the peak positions. (b) Two-dimensional diffraction intensity mapping of the NCO film deposited at 350 °C around the (115) reflection of the MAO substrate. h [110] and l [001] are coordinates in reciprocal space and represent the in-plane and out-of-plane directions, respectively; rlu represents reciprocal lattice unit. (c) X-ray reflectivity (black open circles) and the corresponding fitting results (color solid lines) of NCO films deposited at various T_g. (d) Lattice parameter c calculated from (a) and film thickness extracted from fittings in (c) as a function of T_g, the error bars denote the standard deviation of film thickness.

an example. The (115) reflection of the NCO film shares the same in-plane reciprocal vector with the substrate, indicating that the epitaxial NCO film is coherently grown and fully strained to the substrate. Shown in Fig. 1(c) is the x-ray reflectivity of NCO films deposited at various T_g, with fittings to each line, using film thickness as the fitting parameter. The extracted film thickness is around 12.5 ± 0.2 nm and is almost independent of T_g, as also shown in Fig. 1(d). All the films exhibit a smooth surface with the largest root-mean-square roughness value being only 0.15 nm (see Fig. S1 in Supplemental Material for the surface morphology of films with different T_g [26]).

B. Magnetic characteristics

Figures 2(a) and 2(b) show out-of-plane and in-plane M-H hysteresis loops, respectively, of NCO films deposited at various T_g, measured at 10 K. Diamagnetic contributions from the MAO substrates, acquired by linear fitting to the saturated high field data, are subtracted. In the out-of-plane direction, NCO films show square hysteresis loops with saturated magnetization decreasing from 2.30 to 1.62 μ_B per formula unit (μ_B f.u.$^{-1}$) as T_g increases from 250 to 350 °C. In contrast, the in-plane M-H loops are canted with a much larger saturated magnetic field, confirming the previously reported PMA in epitaxial NCO films [15–22]. The largest out-of-plane saturated magnetization, 2.30 μ_B f.u.$^{-1}$, is observed in NCO films deposited at 250 °C. This is larger than most magnetization values reported for NCO films, and even larger than the value in bulk, approximately 2 μ_B f.u.$^{-1}$ [15–22]. Lüders *et al.* reported an enhanced magnetization in epitaxial $NiFe_2O_4$ films and explained by cation disorder [27]. A similar mechanism may also work in NCO films, where the general formula can be written as $Co_x^{2+}Co_{1-x}^{3+}[Ni_{1-x}^{2+}Ni_x^{3+}Co^{3+}]O_4^{2-}$ $(0 < x < 1)$ [17,28]. The tetrahedral (T_d) sites are occupied by high-spin Co^{2+} and Co^{3+} cations, carrying $3\mu_B$ and $4\mu_B$, respectively. The octahedral (O_h) sites are occupied by high-spin Ni^{2+} with $2\mu_B$, low-spin Ni^{3+} with $1\mu_B$, and diamagnetic low-spin Co^{3+} [17,28]. The spins at each site are aligned in parallel, but the spins at the O_h sites are aligned antiparallel with those at the T_d sites. As a result, a saturation moment of 2 μ_B f.u.$^{-1}$ can be expected irrespective of x [17,28]. An increase of magnetization at the T_d sites, a decrease of magnetization at the O_h sites, or both, may increase the net magnetization.

PMA describes the magnetic anisotropy, in which the direction of easy axes is perpendicular to the film surface. This magnetic anisotropy can be regarded as a field that tends to hold the magnetization in certain equivalent crystallographic directions. To evaluate the PMA properties quantitatively, we estimate the effective PMA constant K_{eff}, which can be deduced from the area enclosed between the magnetization curves with the applied field parallel and perpendicular to the film plane in the first quadrant [3,4]. Figure 3(e) shows that K_{eff} increases generally with the increase of T_g, suggesting the enhanced PMA in samples deposited at higher T_g. The maximum K_{eff} of 5.1 Merg cm^{-3} is comparable to the values reported

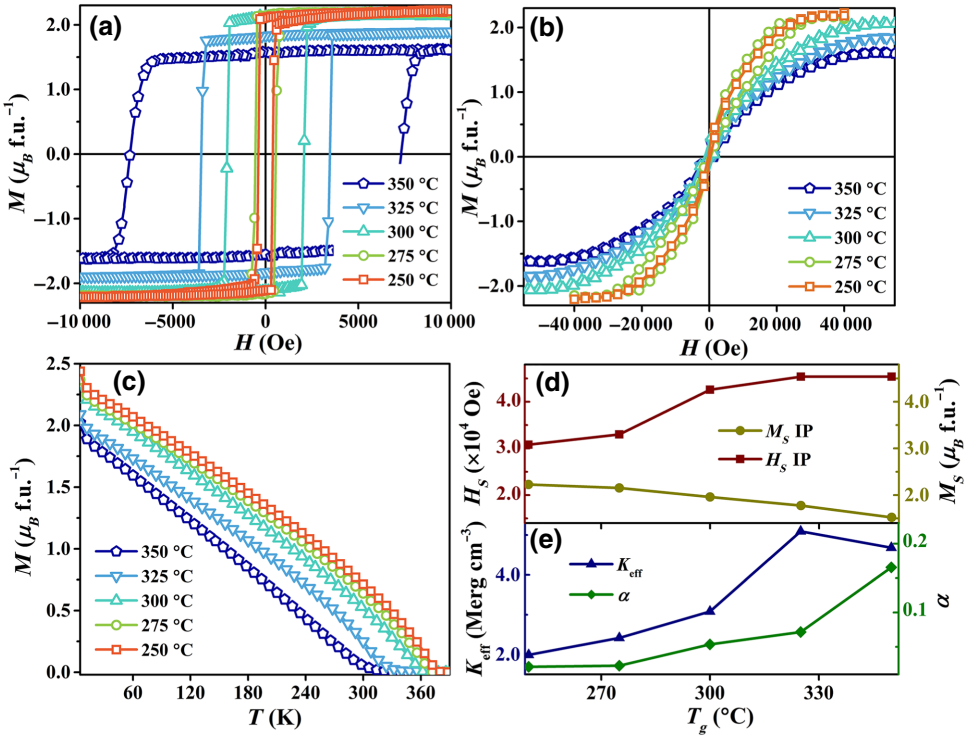

FIG. 2. (a) Out-of-plane and (b) in-plane M-H hysteresis loops measured at 10 K. (c) M-T curves of NCO films deposited at various T_g. (d) In-plane saturation fields (H_s IP) and saturated magnetizations (M_s IP) as functions of T_g. (e) The effective PMA constant K_{eff} and the inhomogenity factor α as functions of T_g.

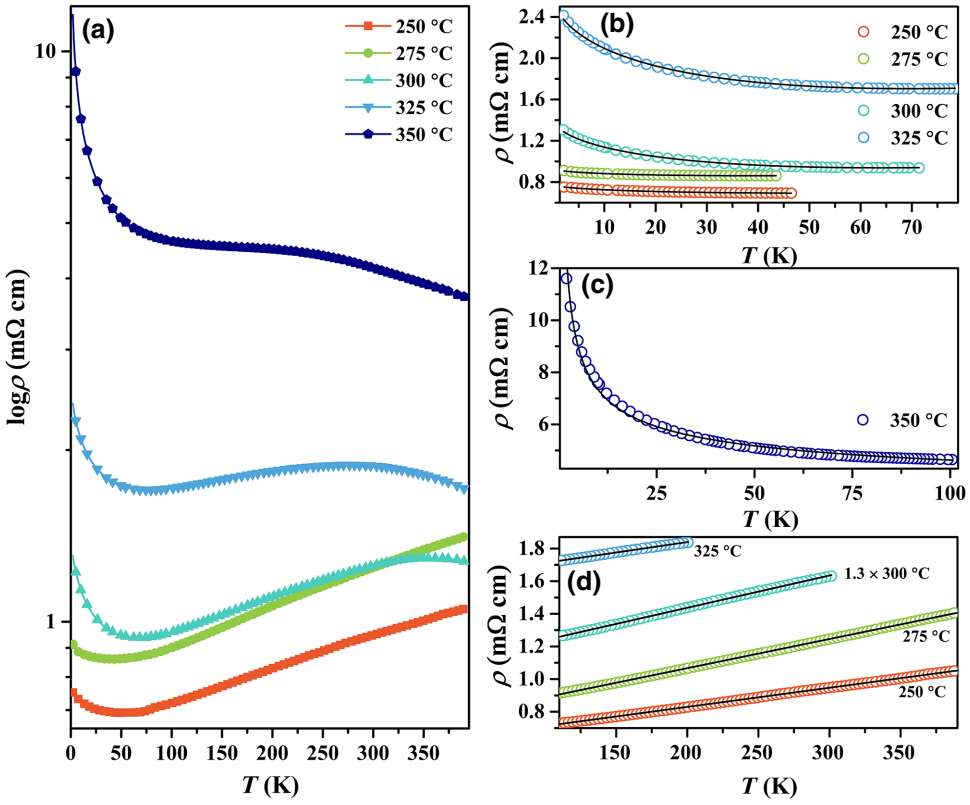

FIG. 3. (a) Temperature dependence of longitudinal resistivity of NCO films deposited at various T_g. (b) Low-temperature resistivity of NCO films deposited at $T_g = 250$, 275, 300, and 325 °C fitted to Eq. (1). (c) Resistivity of NCO film deposited at $T_g = 350$ °C fitted to Eq. (2). (d) Resistivity in the metallic state of NCO films deposited at $T_g = 250$, 275, 300, and 325 °C fitted to Eq. (3). Data for $T_g = 300$ °C are scaled by 1.3 for clarity.

previously in NCO films [29]. PMA is a crucial feature in the design of spintronic devices such as spin transfer torque magnetoresistive random access memories, but it is relatively rare in oxide thin films due to the strong shape anisotropy [3,4,29–31]. For example, $La_{2/3}Sr_{1/3}MnO_3$ thin films usually exhibit an in-plane easy axis. When compressively strained, $La_{2/3}Sr_{1/3}MnO_3$ thin films may show PMA with K_{eff} being only 0.2 Merg cm^{-3} [32,33]. The large K_{eff} observed in the NCO films are beneficial to PMA-based perpendicular magnetic recording.

Another obvious feature in Fig. 2(a) is that the out-of-plane coercive field increases significantly from 350 to 7300 Oe as T_g increases from 250 to 350 °C. The increase of coercivity has often been ascribed to the change of electronic structure and/or pinning by defects. For example, Park *et al.* reported a large reduction in H_c from 4000 to 300 Oe in Fe_3GeTe_2 thin flakes due to Fe deficiency [34]. A wide-range continuous modulation of H_c from 48 to 16 KOe in $SrTiO_3$-capped $SrRuO_3$ films has been attributed to domain pinning and depinning by controlled migration of oxygen vacancies [35]. According to the simplified phenomenological model proposed by Kronmüller [36], $H_c = 2\alpha K_1/M_s - N_{\text{eff}}M_s$, where α is the inhomogeneity factor, representing the influences from the defects acting as pinning centers during domain switching [4,35]. K_1 is the first magnetocrystalline anisotropy constant and can be calculated as $K_1 = 1/2H_sM_s$, where H_s and M_s are the saturation field and saturated magnetization, respectively, measured with the applied field in the film plane [3,4], as shown in Fig. 2(d). N_{eff} is the demagnetization factor related to the shape and the magnetization direction of sample. For NCO films with PMA, N_{eff} can be taken as 1, then α can be calculated [4,35,36]. As shown in Fig. 2(e), α increases monotonically by 7.86 times with T_g increasing from 250 to 350 °C. By comparison, the monotonically increased H_c in NCO films with increasing T_g can be mainly ascribed to the increase of α, which indicates the increased pinning effect of disorder with increasing T_g. The increased disorder at higher T_g is also confirmed by the following transport analysis. Lattice defects, such as cation and oxygen vacancies or antiphase boundaries, may pin domain switching [34–36].

Figure 2(c) shows the out-of-plane M-T curves of the NCO films deposited at various T_g. Diamagnetic contributions from bare MAO substrates are measured and subtracted. Unlike ferromagnetic materials that usually show a sharp increase in magnetization below T_C, the magnetization of NCO films increases at nearly the same rate with decreasing temperature for all the NCO films studied, indicating the ferrimagnetic nature of NCO films [3,4]. T_C, determined by extrapolating the linear dependence to zero magnetization, decreases from 380 to 302 K as T_g increases from 250 to 350 °C. The reduction of T_C may be attributed to the appearance of residual strain, oxygen vacancies, and local disorder in cation distribution, as has often been reported in transition metal oxide thin films [37,38].

C. Transport characteristics

Temperature-dependent longitudinal resistivity of NCO films deposited at various T_g is measured from 2 to 390 K with the current along the [110] direction. In general, the resistivity increases with increasing T_g, as shown in Fig. 3(a). The NCO film deposited at the highest $T_g = 350\,°C$ is insulating in the entire temperature range measured. When deposited at 325 and 300 °C, NCO films show an insulating behavior at high temperature, a metallic behavior in the intermediate temperature, and a reentry into the insulating state at low temperature. The high-temperature transition from the insulating to the metallic state upon cooling occurs at around the ferrimagnetic T_C of the NCO films, obviously associated with the appearance of the long-range magnetic order that facilitates electron hopping, as previously reported [17,19,20,39]. When further decreasing T_g to 275 and 250 °C, the resistivity of NCO films decreases with decreasing temperature until the metal-to-insulator transition occurs at low temperature.

This low-temperature metal-to-insulator transition is observed in all the NCO films deposited at T_g below 350 °C. The transition temperature $T_{\min}$, at which the minimum resistivity occurs, increases from 46 to 78 K as T_g increases from 250 to 325 °C. This kind of low-temperature resistivity upturn has been frequently observed in correlated oxide thin films. For example, the low-temperature metal-to-insulator transition in ultrathin $SrRuO_3$ and $LaNiO_3$ films was explained by weak localization due to quantum interference via electron-electron or election-phonon interactions [40,41]. The increase of resistivity below 47 K in $Mn_{3+x}\,Sn_{1-x}$ thin films was ascribed to the Kondo effect due to the scattering of conduction carriers by the localized spins of magnetic impurities [42]. The mechanism can be extracted by examining the temperature dependence of resistivity. As shown in Fig. 3(b), we fit the resistivity below $T_{\min}$ with [40,41,43]

$$\rho(T) = \rho_0 + aT^{3/4} + bT^n, \tag{1}$$

where ρ_0, a, b, and n are fitting parameters. Equation (1) describes the weak localization due to the disorder-enhanced electron-electron scattering in the dirty limit [43]. ρ_0 is the temperature-independent residual resistivity correlated with defects and impurities. The second term describes the elastic electron-electron scattering and all the inelastic scattering processes due to electron-phonon, electron-magnon, and electron-electron interactions are assumed to be adequately described by a single power law bT^n [40,41,43]. The continuous increase of ρ_0, b, and the absolute value of a indicate the increased disorder and localizations in films deposited at higher T_g (see Fig. S2 in the Supplemental Material for the T_g dependence of fitting parameters in Eq. (1) [26]). Correspondingly, $T_{\min}$ can be interpreted as a representation of the competition between localization induced by the electron-electron scattering and the thermal delocalization. In films deposited at higher T_g, the enhanced localization shifts $T_{\min}$ to higher temperature.

The NCO film deposited at $T_g = 350\,°C$ shows an insulating behavior in the whole temperature range measured. The low-temperature resistivity in this sample can be well fitted to the three-dimensional Mott variable range hopping (VRH) model [19,44,45],

$$\rho(T) = A\exp(T_0/T)^{1/4}, \tag{2}$$

as shown in Fig. 3(c), where A is a constant and T_0 is the VRH characteristic temperature associated with the density of localized states, indicating the increased disorder in the sample with $T_g = 350\,°C$ [19,44,45]. According to Mott [45], carriers hop among localized states, assisted by atomic displacements in the lattice. As the temperature decreases, phonons do not have enough energy to assist hopping, resulting in the increase of resistivity [44,45].

Bulk NCO exhibits a ferrimagnetic metallic behavior with $d\rho/dT > 0$ below T_C [15–22]. NCO films deposited at $T_g \leq 325\,°C$ are metallic in the intermediate temperature region, with a linear resistivity-temperature dependence [46],

$$\rho(T) = \rho_1 + BT, \tag{3}$$

as demonstrated in Fig. 3(d). The linear dependence of $\rho(T)$ is well known as a result of electron-phonon scattering [46]. The residual resistivity ρ_1 and the temperature-independent coefficient B obtained from fitting to Eq. (3) for different T_g are summarized in the Supplemental Material Fig. S3 [26]. The decrease of B for T_g above 275 °C implies the weakened electron-phonon scattering, and the increased ρ_1 suggests the increased amount of disorder in films deposited at higher T_g.

D. Cation coordination and valance analyses

To further understand the transport and magnetic characteristics described above, XPS and XAS measurements are performed to study the electronic structure of Ni and Co cations in NCO films. Figure 4(a) shows the XPS $2p_{3/2}$ core level spectra of Ni cations as functions of T_g. It is observed that the Ni $2p_{3/2}$ peak shifts by 0.5 eV towards lower binding energy as T_g increases from 250 to 350 °C. In NCO, Ni cations predominantly occupy the O_h sites [16–22], and the binding energy shift mainly comes from the variation of Ni valence states [47]. Ni cations with higher valence usually show a higher binding energy [47–49]. Therefore, the downshift in Fig. 4(a) indicates that the average valence of Ni cations decreases, with more Ni^{2+} cations in samples deposited at elevated T_g. By fitting the XPS results in Fig. 4(a) using the peak at 853.78 eV for Ni^{2+}, and the peak at 855.51 eV for Ni^{3+} [47–55], the Ni^{3+} : Ni^{2+} atomic ratio can be obtained as a function of T_g, as shown in Fig. 4(c) (see Supplemental Material for

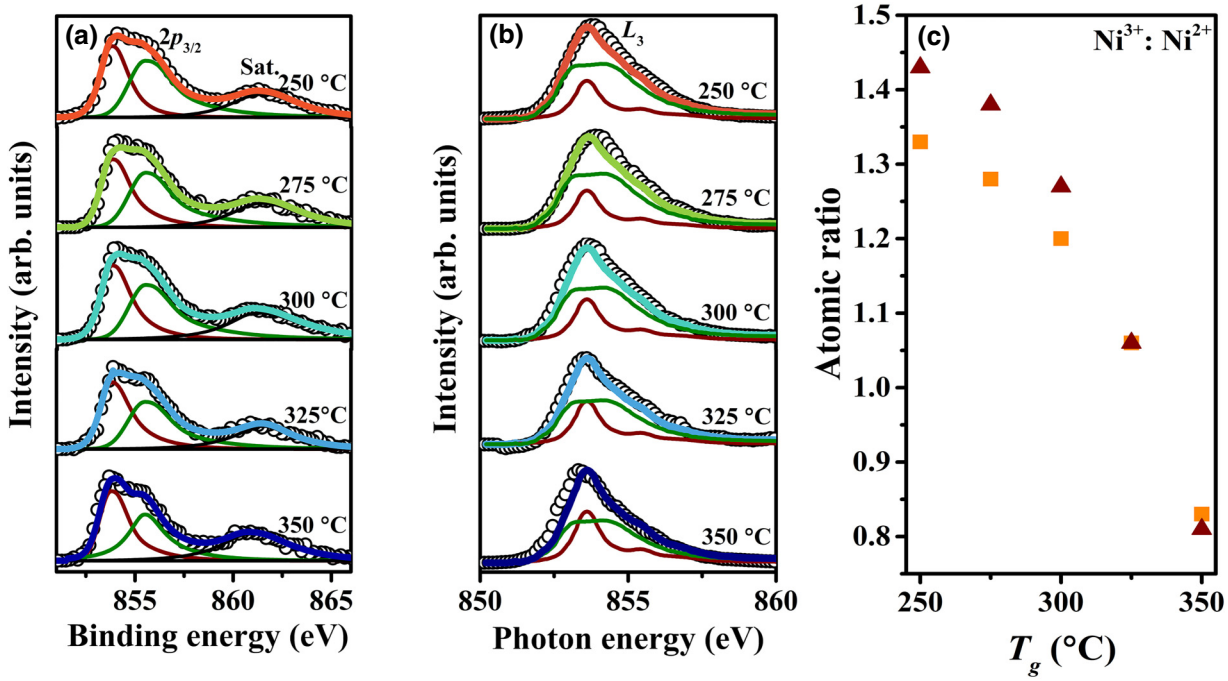

FIG. 4. (a) XPS spectra of Ni $2p_{3/2}$ core level and corresponding fitting results for NCO films deposited at various T_g. The fitting is performed with components at 853.78 eV for Ni^{2+} cations, 855.51 eV for Ni^{3+} cations, and 861.22 eV for the satellite peak (Sat.). (b) XAS spectra of Ni L_3 absorption edge and corresponding fitting results for NCO films deposited at various T_g. The olive curves represent XAS spectra for $Ni^{3+}(O_h)$ from $LaNiO_3$, the wine curves represent XAS spectra for $Ni^{2+}(O_h)$ from NiO. (c) The Ni^{3+} : Ni^{2+} atomic ratio as a function of T_g, acquired from fitting the XPS (orange solid squares) and XAS results (wine solid triangles).

fitting details [26]). The Ni^{3+} : Ni^{2+} atomic ratio is 1.33 when T_g is 250 °C, then decreases to about 0.83 when T_g is 350 °C.

Figure 4(b) shows the Ni L_3 XAS edges for NCO films deposited at various T_g. It is observed that the absorption edge also shifts towards lower energy with increasing T_g. The absorption peak is at 853.8 eV for the $T_g = 250$ °C sample and 853.4 eV for the $T_g = 350$ °C sample, with the full width at half maximum of about 2.8 eV. For Ni^{3+} cations occupying the O_h sites in $LaNiO_3$, for example, the L_3 edge shows a plateau with a full width at half maximum of about 3.5 eV, and the maximum appears at around 854.0 eV [56]. However, Ni^{2+} cations in NiO exhibit a much sharper peak with a full width at half maximum of only about 1.5 eV, and the maximum appears at around 853.0 eV [57]. Therefore, the XAS results also indicate the coexistence of Ni^{2+} and Ni^{3+} cations at O_h sites, the reduced Ni valence states, and the increased amount of Ni^{2+} at O_h sites in NCO films deposited at elevated T_g [56,57]. The Ni^{3+} : Ni^{2+} atomic ratio can also be estimated by fitting the measured Ni L_3 edges with a linear combination of those from $LaNiO_3$ and NiO, as shown in Fig. 4(b) (see Supplemental Material for the fitting details [26]) [58]. According to the relative spectral weight, the Ni^{3+} : Ni^{2+} atomic ratio can be estimated, decreasing with the increase in T_g in good agreement with the XPS results, as also shown in Fig. 4(c). The average valence state of Ni can be estimated, from the Ni^{3+} : Ni^{2+} atomic ratio, as $Ni^{2.59+}$ for the $T_g = 250$ °C sample, and $Ni^{2.45+}$ for the $T_g = 350$ °C sample.

Figure 5(a) shows the Co $2p_{3/2}$ XPS core level spectra of NCO films deposited at various T_g. The peak shifts by 0.4 eV towards lower binding energy as T_g increases from 250 to 350 °C. However, the analysis of the Co XPS chemical shift is much more complex, as not only the valence states but also the coordination correlate with the chemical shift [59,60]. The XPS spectra should be deconvoluted into three peaks representing Co^{2+} on T_d sites, Co^{3+} on T_d sites, and Co^{3+} on O_h sites. However, we try in vain to find a reliable binding energy for Co^{3+} on T_d sites, and therefore, give up on decomposing the Co XPS spectra. We then try to analyze Co valence and coordination by XAS.

Figure 5(b) shows the Co L_3 XAS edges for NCO films deposited at various T_g. The main feature is a broad peak around 780.0 eV. As reported previously, the L_3 absorption peaks of both Co^{3+} at T_d sites and Co^{3+} at O_h sites appear at about 780.2 eV [61–64]. As T_g increases, a shoulder at around 778.0 eV, indicated in Fig. 5(b) by arrows, appears gradually. As proposed by Kan *et al.* [21], this shoulder originates mainly from Co^{2+} at T_d sites in NCO films [22]. Therefore, the concentration of Co^{2+} cations occupying the T_d sites increases with increasing T_g. As shown

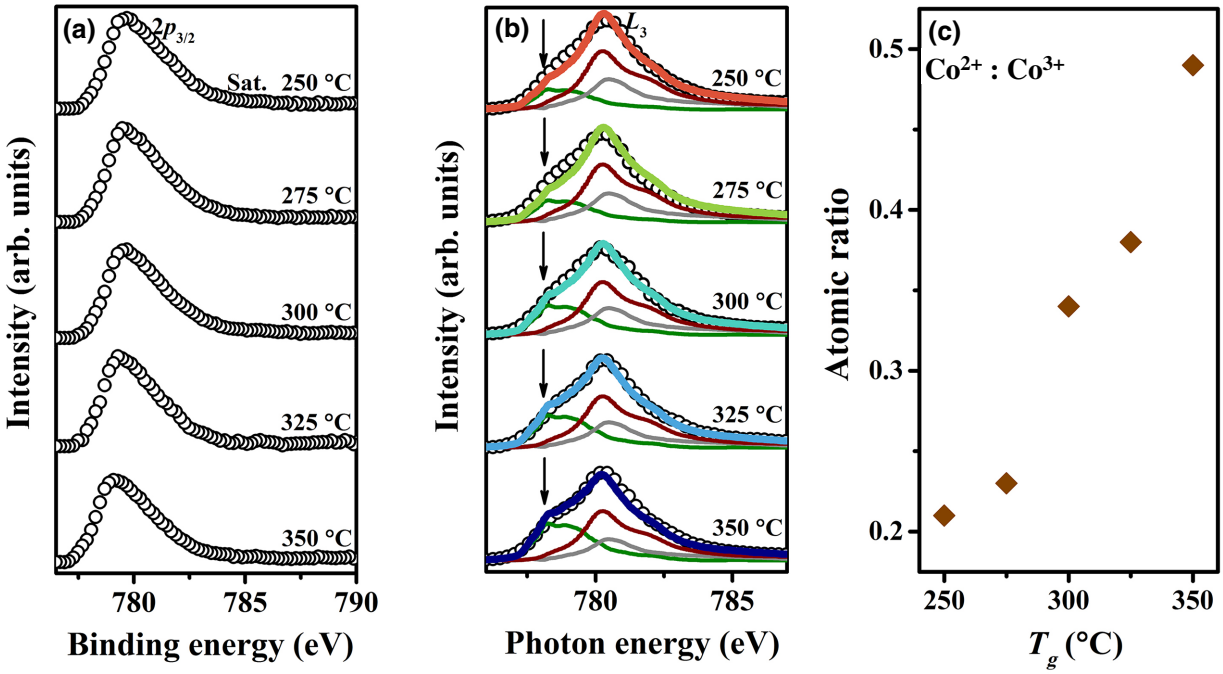

FIG. 5. (a) XPS spectra of Co $2p_{3/2}$ core level for NCO films deposited at various T_g. (b) XAS spectra of Co L_3 absorption edge and corresponding fitting results for NCO films deposited at various T_g. The olive curves represent XAS spectra for Co^{2+} at T_d sites, the grey curves represent XAS spectra for Co^{3+} at T_d sites, and the wine curves represent XAS spectra for Co^{3+} at O_h sites. (c) The Co^{2+} : Co^{3+} atomic ratio as a function of T_g, acquired from fitting the XAS results.

in Fig. 5(b), the Co L_3 edges of the NCO films can be well fitted with a linear combination of the L_3 edges of Co^{2+} at T_d sites, Co^{3+} at T_d sites, and Co^{3+} at O_h sites (see Supplemental Material for fitting details [26]) [17,58,61–64]. Based on the relative spectral weights, the relative fraction of Co^{2+} at T_d sites, Co^{3+} at T_d sites, and Co^{3+} at O_h sites can be estimated. It is, for example, 0.35:0.45:1.2 for the $T_g = 250$ °C sample. With increasing T_g, the number of Co cations at the T_d sites increases while that at O_h decreases. It becomes 0.66:0.32:1.02 for the $T_g = 350$ °C sample. As a result, the Co^{2+} : Co^{3+} atomic ratio increases from 0.21 to 0.49, as shown in Fig. 5(c), and the average valence state decreases from $Co^{2.83+}$ to $Co^{2.67+}$ with T_g increasing from 250 to 350 °C. Although Co^{3+} at O_h sites were frequently assumed in the low-spin state [15–22,28], the XAS component of Co^{3+} at O_h sites can be well represented by XAS from Co^{3+} in $LaCoO_3$. As well known in $LaCoO_3$, Co^{3+} cations are only in the low-spin state at very low temperatures [63,64], thus it is reasonable that Co^{3+} cations at the O_h sites are in a mixture of low- and high-spin states at room temperature.

E. Discussions

The variation in cation valence and coordination in NCO films with increasing T_g has profound influences on the structure, magnetic, and transport properties of NCO films. At O_h sites, the atomic radius of a Ni^{2+} cation is 0.69 Å, much larger than that of Ni^{3+} cation (0.53 Å) [19,20]. The continuous increase of Ni^{2+} concentration with increasing T_g may lead to a systematic increase in lattice parameters. At the same time, the increased Co^{2+} and the decreased Co^{3+} concentration at the T_d sites also contributes to the lattice expansion, with the atomic radius being 0.72 Å for the former and 0.61 Å for the latter [65,66]. Lattice expansion shown in Fig. 1(a) results in larger compressive strain in NCO films with higher T_g. The strain modifies the local environment of magnetic ions through the magnetoelastic effect, changing their preferred spin orientations due to spin-orbit coupling [21,22,29]. Recent works pointed out that among the magnetic ions in NCO films, Co cations at T_d sites play a key role in determining the PMA, while the contribution of Ni ions is less dominant. This is because of the large orbital moment of the in-plane Co $3d_{x^2-y^2}$ state and the magnetoelastic effect due to the compressive strain. According to the analysis above, Co concentration at the T_d sites increases in NCO films deposited at higher T_g. The increased Co concentration, together with the increased compressive strain, results in the enhanced PMA observed in Fig. 2(e), which inevitably leads to a larger H_c. As for the transport property, recent experimental results and first-principles calculations have shown that the Fermi surface in NCO is composed of spin-down electrons of Ni cations at the O_h sites, making NCO

half-metallic [17,67,68]. The appearance of Ni^{3+} at the O_h sites provides a partially occupied e_g orbital and facilitates carrier transport through Ni^{2+}-O-Ni^{3+} and Co^{2+}-O-Ni^{3+} [17,67,68]. At the same time, Co at either T_d or O_h sites provides almost no density of states at the Fermi level and has less influence on electrical conduction in NCO films [17,68]. Hence, having fewer Ni^{3+} cations in NCO is detrimental to carrier transport. The resistivity of NCO films increases with increasing T_g, which leads to a higher concentration of Ni^{2+} cations in the films. For magnetization, assuming Co^{3+} cations at the O_h sites are completely in the low-spin state, providing no magnetization, the obtained cation concentration, as shown in Figs. 4(c) and 5(c), generates a total magnetization increasing with the increase of T_g, contrary to the observation in Fig. 2. However, deposition at higher T_g induces more defects, as concluded from the analysis of resistivity. These defects inevitably have effects on not only the transport, but also the structure and magnetic properties. The concentration of oxygen vacancies can be estimated based on charge neutrality, being 1.25%, 2.25%, and 2.75% for samples with $T_g = 275$, 325, and 350 °C, respectively, suggesting the increased oxygen vacancy concentration at higher T_g. It has been well documented that oxygen vacancies may lead to the reduction of magnetization by disturbing the double exchange interaction, which may occur in NCO films and lead to the decreased magnetization [69,70].

IV. CONCLUSION

In summary, epitaxial NCO films, with large PMA, are deposited on single-crystalline MAO (001) substrates by pulsed laser deposition at various T_g. The out-of-plane H_c can be tuned systematically by about 20 times from 350 to 7300 Oe with T_g increasing from 250 to 350 °C. Such a significant H_c tunability can be explained by the increased concentration of defects and the enhanced PMA in NCO films as T_g increases. Based on XPS and XAS analyses, the variations of magnetic and transport characteristics are attributed to the variation of the valence and coordination of Ni and Co cations as functions of deposition temperature. These results are helpful to the optimization and application of NCO films for multifunctional magnetic devices.

ACKNOWLEDGMENTS

This work was jointly supported by National Natural Science Foundation of China (Grants No. 11874207, No. 51725203, No. 51721001, and No. U1932115) and the National Key R&D Program of China (Grant No. 2020YFA0711504). The authors acknowledge the MCD-A, MCD-B (Soochow Beamline for Energy Materials) and BL11U beamlines at National Synchrotron Radiation Laboratory (Hefei, China) for the XAS measurement.

[1] S. Hirosawa, M. Nishino, and S. Miyashita, Perspectives for high-performance permanent magnets: applications, coercivity, and new materials, Adv. Nat. Sci.: Nanosci. Nanotechnol. **8**, 013002 (2017).

[2] E. A. Gorbachev, E. S. Kozlyakova, L. A. Trusov, A. E. Sleptsova, M. A. Zykin, and P. E. Kazin, Design of modern magnetic materials with giant coercivity, Russ. Chem. Rev. **90**, 1287 (2021).

[3] B. D. Cullity and C. D. Graham, *Introduction to magnetic materials* (John Wiley & Sons. Inc., Hoboken, New Jersey, USA, 2009).

[4] J. M. D. Coey, *Magnetism and magnetic materials* (Cambridge University Press, Cambridge, UK, 2010).

[5] L. Fallarino, M. Quintana, E. L. Rojo, and A. Berger, Suppression of Coercivity in Nanoscale Graded Magnetic Materials, Phys. Rev. Lett. **16**, 034038 (2021).

[6] G. F. Liu, Z. D. Zhang, F. Dang, C. B. Cheng, C. X. Hou, and S. D. Liu, Formation and characterization of magnetic barium ferrite hollow fibers with low coercivity via co-electrospun, J. Magn. Magn. Mater. **412**, 55 (2016).

[7] L. J. Zhu, S. H. Nie, K. K. Meng, D. Pan, J. H. Zhao, and H. Z. Zheng, Multifunctional $L1_0$-$Mn_{1.5}Ga$ films with ultrahigh coercivity, giant perpendicular magnetocrystalline anisotropy and large magnetic energy product, Adv. Mater. **24**, 4547 (2012).

[8] W. A. Challener, C. B. Peng, A. V. Itagi, D. Karns, W. Peng, Y. G. Peng, X. M. Yang, X. B. Zhu, N. J. Gokemeijer, Y.-T. Hsia, *et al.*, Heat-assisted magnetic recording by a near-field transducer with efficient optical energy transfer, Nat. Photon. **3**, 220 (2009).

[9] A. R. Balakrishna and R. D. James, A tool to predict coercivity in magnetic materials, Acta Mater. **208**, 116697 (2021).

[10] Y. F. Wei, P. Nukala, M. Salverda, S. Matzen, H. J. Zhao, J. Momand, A. S. Everhardt, G. Agnus, G. R. Blake, P. Lecoeur, *et al.*, A rhombohedral ferroelectric phase in epitaxially strained $Hf_{0.5}Zr_{0.5}O_2$ thin films, Nat. Mater. **17**, 1095 (2018).

[11] S. Yoon, X. Gao, J. M. Ok, Z. L. Liao, M.-G. Han, Y. M. Zhu, P. Ganesh, M. F. Chisholm, W. S. Choi, and H. N. Lee, Strain-induced atomic-scale building blocks for ferromagnetism in epitaxial $LaCoO_3$, Nano Lett. **21**, 4006 (2021).

[12] Z. Chen, Y. Liu, H. Zhang, Z. R. Liu, H. Tian, Y. Q. Sun, M. Zhang, Y. Zhou, J. R. Sun, and Y. W. Xie, Electric field control of superconductivity at the $LaAlO_3/KTaO_3(111)$ interface, Science **372**, 721 (2021).

[13] L. Vistoli, W. B. Wang, A. Sander, Q. X. Zhu, B. Casals, R. Cichelero, A. Barthélémy, S. Fusil, G. Herranz, S. Valencia, *et al.*, Giant topological Hall effect in correlated oxide thin films, Nat. Phys. **15**, 67 (2019).

[14] B. Göbel, I. Mertig, and O. A. Tretiakov, Beyond skyrmions: Review and perspectives of alternative magnetic quasiparticles, Phys. Rep. **895**, 1 (2021).

[15] P. Silwal, L. D. Miao, I. Stern, X. L. Zhou, J. Hu, and D. H. Kim, Metal insulator transition with ferrimagnetic order in epitaxial thin films of spinel $NiCo_2O_4$, Appl. Phys. Lett. **100**, 032102 (2012).

[16] M. N. Iliev, P. Silwal, B. Loukya, R. Datta, D. H. Kim, N. D. Todorov, N. Pachauri, and A. Gupta, Raman studies of

cation distribution and thermal stability of epitaxial spinel $NiCo_2O_4$ films, J. Appl. Phys. **114**, 033514 (2013).

[17] Y. Bitla, Y.-Y. Chin, J.-C. Lin, C. N. Van, R. R. Liu, Y. M. Zhu, H.-J. Liu, Q. Zhan, H.-J. Lin, C.-T. Chen, *et al.*, Origin of metallic behavior in $NiCo_2O_4$ ferrimagnet, Sci. Rep. **5**, 15201 (2015).

[18] H. Sharona, B. Loukya, U. Bhat, R. Sahu, B. Vishal, P. Silwal, A. Gupta, and R. Datta, Coexisting nanoscale inverse spinel and rock salt crystallographic phases in $NiCo_2O_4$ epitaxial thin films grown by pulsed laser deposition, J. Appl. Phys. **122**, 225301 (2017).

[19] W. Z. Guo, C. M. Zhen, C. F. Wu, X. C. Wu, G. K. Li, L. Ma, and D. L. Hou, Influence of growth temperature on the microstructure and electrical transport properties of epitaxial $NiCo_2O_4$ thin films, Ceram. Inter. **44**, 12539 (2018).

[20] K. Q. Zhang, C. M. Zhen, W. G. Wei, W. Z. Guo, G. D. Tang, L. Ma, D. L. Hou, and X. C. Wu, Insight into metallic behavior in epitaxial halfmetallic $NiCo_2O_4$ films, RSC Adv. **7**, 36026 (2017).

[21] D. Kan, M. Mizumaki, M. Kitamura, Y. Kotani, Y. F. Shen, I. Suzuki, K. Horiba, and Y. Shimakawa, Spin and orbital magnetic moments in perpendicularly magnetized $Ni_{1-x}Co_{2+y}O_{4-z}$ epitaxial thin films: Effects of site-dependent cation valence states, Phys. Rev. B **101**, 224434 (2020).

[22] I. Suzuki, D. Kan, M. Kitamura, Y. F. Shen, K. Horiba, and Y. Shimakawa, Influence of oxygen vacancies on magnetic properties of perpendicularly magnetized $NiCo_2O_4$ epitaxial thin films, J. Appl. Phys. **127**, 203903 (2020).

[23] N. Jaber, J. Wolfman, C. Daumont, B. Négulescu, A. Ruyter, T. Sauvage, B. Courtois, H. Bouyanfif, J. L. Longuet, C. Autret-Lambert, and F. Gervais, Laser fluence and spot size effect on compositional and structural properties of $BiFeO_3$ thin films grown by Pulsed Laser Deposition, Thin Solid Films **634**, 107 (2017).

[24] M. N. Grisolia, F. Y. Bruno, D. Sando, H. J. Zhao, E. Jacquet, X. M. Chen, L. Bellaiche, A. Barthélémy, and M. Bibes, Structural, magnetic, and electronic properties of $GdTiO_3$ Mott insulator thin films grown by pulsed laser deposition, Appl. Phys. Lett. **105**, 172402 (2014).

[25] H. M. Ifkekhar Jaim, S. H. Lee, X. H. Zhang, and I. Takeuchi, Stability of the oxygen vacancy induced conductivity in $BaSnO_3$ thin films on $SrTiO_3$, Appl. Phys. Lett. **111**, 172102 (2017).

[26] See the Supplemental Material at http://link.aps.org/supplemental/10.1103/PhysRevApplied.18.014008 for surface morphology, T_g dependence of fitting coefficients used in Eqs. (1) and (3), and fitting details for XPS and XAS analysis.

[27] U. Lüders, M. Bibes, J.-F. Bobo, M. Cantoni, R. Bertacco, and J. Fontcuberta, Enhanced magnetic moment and conductive behavior in $NiFe_2O_4$ spinel ultrathin films, Phys. Rev. B **71**, 134419 (2005).

[28] X. G. Chen, X. Z. Zhang, M.-G. Han, L. Zhang, Y. M. Zhu, X. S. Xu, and X. Hong, Magnetotransport anomaly in room-temperature ferrimagnetic $NiCo_2O_4$ thin films, Adv. Mater. **31**, 1805260 (2019).

[29] C. Mellinger, J. Waybright, X. Z. Zhang, C. Schmidt, and X. S. Xu, Perpendicular magnetic anisotropy in conducting $NiCo_2O_4$ films from spin-lattice coupling, Phys. Rev. B **101**, 014413 (2020).

[30] A. Sahoo, W. Prellier, and P. Padhan, Ultrathin scale tailoring of anisotropic magnetic coupling and anomalous magnetoresistance in $SrRuO_3-PrMnO_3$ superlattices, ACS Appl. Mater. Interfaces **10**, 44190 (2018).

[31] Z. T. Zeng, J. T. Feng, X. Zheng, C. H. Wang, J. W. Liu, Z. X. Lu, F. X. Jiang, X. H. Xu, Z. M. Wang, and R. W. Li, Emergent ferromagnetism with tunable perpendicular magnetic anisotropy in short-periodic $SrIrO_3/SrRuO_3$ superlattices, Appl. Phys. Lett. **116**, 142401 (2020).

[32] Z. Y. Xiao, F. Zhang, M. A. Farrukh, R. Wang, G. W. Zhou, Z. Y. Quan, and X. H. Xu, Perpendicular magnetic anisotropy in compressive strained $La_{0.67}Sr_{0.33}MnO_3$ films, J. Mater. Sci. **54**, 9017 (2019).

[33] Y. Wu, Y. Suzuki, U. Rüdiger, J. Yu, A. D. Kent, T. K. Nath, and C. B. Eom, Magnetotransport and magnetic domain structure in compressively strained colossal magnetoresistance films, Appl. Phys. Lett. **75**, 2295 (1999).

[34] S. Y. Park, D. S. Kim, Y. Liu, J. Hwang, Y. Kim, W. Kim, J.-Y. Kim, C. Petrovic, C. Hwang, S.-K. Mo, *et al.*, Controlling the magnetic anisotropy of the van der Waals ferromagnet Fe_3GeTe_2 through hole doping, Nano Lett. **20**, 95 (2020).

[35] E. K. Ko, J. Mun, H. G. Lee, J. Kim, J. Song, S. H. Chang, T. H. Kim, S. B. Chung, M. Kim, L. F. Wang, and T. W. Noh, Oxygen vacancy engineering for highly tunable ferromagnetic properties: a case of $SrRuO_3$ ultrathin film with a $SrTiO_3$ capping layer, Adv. Funct. Mater. **30**, 2001486 (2020).

[36] H. Kronmüller, Theory of nucleation fields in inhomogeneous ferromagnets, Phys. Status Solidi B **144**, 385 (1987).

[37] R. Nori, S. N. Kale, U. Ganguly, N. R. C. Raju, D. S. Sutar, R. Pinto, and V. R. Rao, Morphology and curie temperature engineering in crystalline $La_{0.7}Sr_{0.3}MnO_3$ films on Si by pulsed laser deposition, J. Appl. Phys. **115**, 033518 (2014).

[38] J. Dho, N. H. Hur, I. S. Kim, and Y. K. Park, Oxygen pressure and thickness dependent lattice strain in $La_{0.7}Sr_{0.3}MnO_3$ films, J. Appl. Phys. **94**, 7670 (2003).

[39] A. Urushibara, Y. Moritomo, T. Arima, A. Asamitsu, G. Kido, and Y. Tokura, Insulator-metal transition and giant magnetoresistance in $La_{1-x}Sr_xMnO_3$, Phys. Rev. B **51**, 14103 (1995).

[40] X. Shen, X. B. Qiu, D. Su, S. Q. Zhou, A. D. Li, and D. Wu, Thickness-dependent metal-insulator transition in epitaxial $SrRuO_3$ ultrathin films, J. Appl. Phys. **117**, 015307 (2015).

[41] P. Scherwitzl, S. Gariglio, M. Gabay, P. Zubko, M. Gibert, and J.-M. Triscone, Metal-Insulator Transition in Ultrathin $LaNiO_3$ Films, Phys. Rev. Lett. **106**, 246403 (2011).

[42] D. Khadka, T. R. Thapaliya, S. H. Parra, X. Y. Han, J. J. Wen, R. F. Need, P. Khanal, W. G. Wang, J. D. Zang, J. M. Kikkawa, *et al.*, Kondo physics in antiferromagnetic Weyl semimetal $Mn_{3+x}Sn_{1-x}$ films, Sci. Adv. **6**, eabc1977 (2020).

[43] P. Silwal, L. D. Miao, J. Hu, L. Spinu, D. H. Kim, and D. Talbayev, Thickness dependent structural, magnetic, and electronic properties of the epitaxial films of transparent conducting oxide $NiCo_2O_4$, J. Appl. Phys. **114**, 103704 (2013).

[44] L. F. Hu, L. M. Wu, M. Y. Liao, X. H. Hu, and X. S. Fang, Electrical transport properties of large, individual $NiCo_2O_4$ nanoplates, Adv. Funct. Mater. **22**, 998 (2012).

[45] N. F. Mott, Conduction in non-crystalline materials, Philos. Mag. **19**, 835 (1969).

[46] G. P. Mambrini, E. R. Leite, M. T. Escote, A. J. Chiquito, E. Longo, J. A. Varela, and R. F. Jardim, Structural, microstructural, and transport properties of highly oriented $LaNiO_3$ thin films deposited on $SrTiO_3$ (100) single crystal, J. Appl. Phys. **102**, 043708 (2007).

[47] Z. W. Fu, J. T. Hu, W. L. Hu, S. Y. Yang, and Y. F. Luo, Quantitative analysis of Ni^{2+}/Ni^{3+} in $Li[Ni_xMn_yCo_z]O_2$ cathode materials: non-linear least-squares fitting of XPS spectra, Appl. Surf. Sci. **439**, 569 (2018).

[48] J. X. Feng, S. H. Ye, A. L. Wang, X. F. Lu, Y. X. Tong, and G. R. Li, Flexible cellulose paper-based asymmetrical thin film supercapacitors with high-performance for electrochemical energy storage, Adv. Funct. Mater. **24**, 7093 (2014).

[49] J. F. Li, S. L. Xiong, Y. R. Liu, Z. C. Ju, and Y. T. Qian, High electrochemical performance of monodisperse $NiCo_2O_4$ mesoporous microspheres as an anode material for Li-ion batteries, ACS Appl. Mater. Interfaces **5**, 981 (2013).

[50] A. C. Pebley, E. Decolvenaere, T. M. Pollock, and M. J. Gordon, Oxygen evolution on Fe-doped NiO electrocatalysts deposited via microplasma, Nanoscale **9**, 15070 (2017).

[51] C. Hu, X. J. Wang, T. Yao, T. L. Gao, J. C. Han, X. H. Zhang, Y. M. Zhang, P. Xu, and B. Song, Enhanced electrocatalytic oxygen evolution activity by tuning both the oxygen vacancy and orbital occupancy of B-site metal cation in $NdNiO_3$, Adv. Funct. Mater. **29**, 1902449 (2019).

[52] S. D. Liu, D. X. Ni, H. F. Li, K. N. Hui, C. Y. Ouyang, and S. C. Jun, Effect of cation substitution on the pseudocapacitive performance of spinel cobaltite MCo_2O_4 (M = Mn, Ni, Cu, and Co), J. Mater. Chem. A **6**, 10674 (2018).

[53] M. Prabu, K. Ketpang, and S. Shanmugam, Hierarchical nanostructured $NiCo_2O_4$ as an efficient bifunctional non-precious metal catalyst for rechargeable zinc–air batteries, Nanoscale **6**, 3173 (2014).

[54] Y. Lei, J. Li, Y. Y. Wang, L. Gu, Y. F. Chang, H. Y. Yuan, and D. Xiao, Rapid microwave-assisted green synthesis of 3D hierarchical flower-shaped $NiCo_2O_4$ microsphere for high-performance supercapacitor, ACS Appl. Mater. Interfaces **6**, 1773 (2014).

[55] G. Li, W. Y. Li, K. B. Xu, R. J. Zou, Z. G. Chen, and J. Q. Hu, Sponge-like $NiCo_2O_4/MnO_2$ ultrathin nanoflakes for supercapacitor with high-rate performance and ultra-long cycle life, J. Mater. Chem. A **2**, 7738 (2014).

[56] H. Guo, Z. W. Li, L. Zhao, Z. Hu, C. F. Chang, C.-Y. Kuo, W. Schmidt, A. Piovano, T. W. Pi, O. Sobolev, *et al.*, Antiferromagnetic correlations in the metallic strongly correlated transition metal oxide $LaNiO_3$, Nat. Commun. **9**, 43 (2018).

[57] J. Lüder, J. Schött, B. Brena, M. W. Haverkort, P. Thunström, O. Eriksson, B. Sanyal, I. D. Marco, and Y. O. Kvashnin, Theory of *L*-edge spectroscopy of strongly correlated systems, Phys. Rev. B **96**, 245131 (2017).

[58] Z. Y. Guo, C. X. Li, M. Gao, X. Han, Y.-J. Zhang, W.-J. Zhang, and W. W. Li, Mn-O covalency governs the intrinsic activity of Co-Mn spinel oxides for boosted peroxymonosulfate activation, Angew. Chem. Int. Ed. **60**, 274 (2021).

[59] J. P. Bonnelle, J. Grimbolt, and A. D. Huysser, Influence de la polarisation des liaisons sur les spectres esca des oxydes de cobalt, J. Electron Spectrosc. Relat. Phenom. **7**, 151 (1975).

[60] M. Fantauzzi, F. Secci, M. S. Angotzi, C. Passiu, C. Cannas, and A. Rossi, Nanostructured spinel cobalt ferrites: Fe and Co chemical state, cation distribution and size effects by X-ray photoelectron spectroscopy, RSC Adv. **9**, 9171 (2019).

[61] N. Hollmann, Z. Hu, M. Valldor, A. Maignan, A. Tanaka, H. H. Hsieh, H.-J. Lin, C. T. Chen, and L. H. Tjeng, Electronic and magnetic properties of the kagome systems $YBaCo_4O_7$ and $YBaCo_3MO_7$ (M = Al, Fe), Phys. Rev. B **80**, 085111 (2019).

[62] C. F. Chang, Z. Hu, H. Wu, T. Burnus, N. Hollmann, M. Benomar, T. Lorenz, A. Tanaka, H.-J. Lin, H. H. Hsieh, *et al.*, Spin Blockade, Orbital Occupation, and Charge Ordering in $La_{1.5}Sr_{0.5}CoO_4$, Phys. Rev. Lett. **102**, 116401 (2009).

[63] M. Abbate, J. C. Fuggle, A. Fujimori, L. H. Tjeng, C. T. Chen, R. Potze, G. A. Sawatzky, H. Eisaki, and S. Uchida, Electronic structure and spin-state transition of $LaCoO_3$, Phys. Rev. B **47**, 16124 (1993).

[64] M. W. Haverkort, Z. Hu, J. C. Cezar, T. Burnus, H. Hartmann, M. Reuther, C. Zobel, T. Lorenz, A. Tanaka, N. B. Brookers, *et al.*, Spin State Transition in $LaCoO_3$ Studied Using Soft X-Ray Absorption Spectroscopy and Magnetic Circular Dichroism, Phys. Rev. Lett. **97**, 176405 (2006).

[65] S. M. Kabbur, D. Y. Nadargi, R. C. Kambale, U. R. Ghodake, and S. S. Suryavanshi, Microstructure and magnetic interactions of Co^{2+} substituted NiCuZn ferrites, J. Magn. Magn. Mater. **517**, 167376 (2021).

[66] M. A. Amer, T. M. Meaz, A. G. Mostafa, M. El-Kastawi, and A. I. Ghoneim, Characterization and spectral studies of Co^{3+}-doped $Cd_{0.4}Mn_{0.6}Fe_2O_4$ ferrites, Ceram. Inter. **241**, 40 (2014).

[67] X. Shi, S. L. Bernasek, and A. Selloni, Formation, electronic structure, and defects of Ni substituted spinel cobalt oxide: a DFT + U study, J. Phys. Chem. C **120**, 14892 (2016).

[68] Y. F. Shen, D. Kan, Z. H. Tan, Y. Wakabayashi, and Y. Shimakawa, Tuning of ferrimagnetism and perpendicular magnetic anisotropy in $NiCo_2O_4$ epitaxial films by the cation distribution, Phys. Rev. B **101**, 094412 (2020).

[69] L. Cao, O. Petracic, P. Zakalek, A. Weber, U. Rücker, J. Schubert, A. Koutsioubas, S. Mattauch, and T. Brückel, Reversible control of physical properties via an oxygen-vacancy-driven topotactic transition in epitaxial $La_{0.7}Sr_{0.3}MnO_{3-\delta}$ thin films, Adv. Mater. **31**, 1806183 (2019).

[70] S. Kumari, N. Mottaghi, C.-Y. Huang, R. Trappen, G. Bhandari, S. Yousefi, G. Cabrera, M. S. Seehra, and M. B. Holcomb, Effects of oxygen modification on the structural and magnetic properties of highly epitaxial $La_{0.7}Sr_{0.3}MnO_3$ (LSMO) thin films, Sci. Rep. **10**, 3659 (2020).